CrossMark

Band gap narrowing and photocatalytic studies of Nd^{3+} ion-doped SnO_2 nanoparticles using solar energy

DHANYA CHANDRAN[1], LAKSHMI S NAIR[1], S BALACHANDRAN[2,*], K RAJENDRA BABU[1] and M DEEPA[3]

[1]Department of Physics, Mahatma Gandhi College, Kerala University, Pattom Palace P.O., Thiruvananthapuram 695 004, India
[2]Department of Chemistry, Mahatma Gandhi College, Kerala University, Pattom Palace P.O., Thiruvananthapuram 695 004, India
[3]Department of Physics, All Saints' College, Kerala University, Chackai P.O., Thiruvananthapuram 695 007, India

Abstract. Pure and Nd^{3+}-doped tin oxide (SnO_2) nanoparticles have been prepared by the sol–gel method and characterized by X-ray diffraction (XRD), transmission electron microscopy (TEM), high-resolution TEM, energy-dispersive spectroscopy and UV–visible spectroscopy. The XRD patterns of all the samples are identified as tetragonal rutile-type SnO_2 phase which is further confirmed by TEM analysis. Neodymium doping introduces band gap narrowing in the prepared samples and enhances their absorption towards the visible-light region. The photocatalytic activity of all the samples was evaluated by monitoring the degradation of methylene blue solution under day light illumination and it was found that the photocatalytic activity significantly increases for the samples calcined at 600 than 400°C, which is due to the effective charge separation of photogenerated electron–hole pairs. The efficiency of photocatalysts was found to be related to neodymium doping percentage and calcination temperature.

Keywords. Band gap narrowing; photocatalytic activity; sol–gel process; tin oxide.

1. Introduction

Dyes are widely used in a variety of industries such as textile, plastic, paper, printing, etc.; consequently they become a common industrial pollutant during their synthesis and applications. The disposal of waste water containing industrial dye has become a major threat for the ecosystem since most of the dyes are non-biodegradable, toxic and even carcinogenic in nature. Among the physicochemical technologies available for the treatment of industrial dye effluents, advanced oxidation processes involving heterogeneous photocatalytic processes using semiconductor nanocrystals as photocatalyst is one of the most efficient methods for the complete degradation of organic dyes [1]. However, due to the large band gap of most of the semiconductors such as SnO_2 (3.6 eV), TiO_2 (3.2 eV) and ZnO (3.3 eV), these materials limit the use of visible light and can be photoactivated only by UV irradiation which constitute only 4–5% of the entire solar energy. Furthermore, the fast recombination of electron–hole pairs in semiconductors reduces the efficiency of photocatalytic reaction. These limitations can be overcome by doping the semiconductors with lanthanide ions/transition metal ions [2–7] or by the coupled semiconductor technique [8,9].

Tin oxide is regarded as one of the most promising semiconductors because of its unique optical, electronic and catalytic properties. It is an n-type semiconductor with a wide band gap of 3.6 eV and has been used in a large range of technological applications due to its tailor-made properties. They have found diverse applications in gas sensors [10], optoelectronic devices [11], solar cells [12] and lithium-ion batteries [13]. In recent years, SnO_2 has gained much interest in the area of photocatalysis because of its high photochemical stability, strong oxidizing power, low cost and non-toxic nature. Singh *et al* [14] reported the photocatalytic activity of Sm^{3+} ion-doped SnO_2 nanoparticles using UV light in the degradation of triphenylmethane dyes (ethyl violet and brilliant green). Foletto *et al* [15] studied the degradation of organic dye used in the leather industry using nanocomposites of CeO_2–SnO_2 under sunlight irradiation.

Many synthetic strategies have been developed for the synthesis of SnO_2 nanoparticles such as the sol–gel method [16], thermal decomposition method [17], chemical precipitation technique [18], solvothermal method [19], chemical vapour deposition method [20], etc. Among the various methods, sol–gel method offers several advantages such as high purity, better homogeneity, precise control over the stoichiometry, phase-pure powders at a lower temperature, ability to control the grain size and capability in controlling the textural and surface properties of metal oxides. In the present paper, pure and neodymium-doped SnO_2 nanoparticles have been prepared through the sol–gel method and their application towards the photocatalytic degradation of methylene blue (MB) was investigated under day light illumination. To the

*Author for correspondence (sbcnair@gmail.com)

best of our knowledge, not a lot of work has been reported in the photodegradation of MB by neodymium-doped SnO_2 using sunlight as a source.

2. Experimental

2.1 *Materials*

The chemicals used in this study were stannic chloride pentahydrate ($SnCl_4 \cdot 5H_2O$, Sigma-Aldrich, USA), ammonium hydroxide (NH_4OH 25%, Merck, Germany), neodymium nitrate hexahydrate ($Nd(NO_3)_3 \cdot 6H_2O$, Merck, Germany), and methylene blue (MB, Merck, Germany). All reagents were used as received without any further purification and double distilled water was used throughout the experiments.

2.2 *Synthesis of pure and Nd^{3+}-doped SnO_2 nanoparticles*

Sol–gel method is employed for the preparation of pure and Nd^{3+}-doped SnO_2 nanopowders. For undoped sample, 5.8 g of tin (IV) chloride was dissolved in 100 ml ultrapure water and stirred for half an hour. The sol was prepared by the dropwise addition of 25% ammonia solution under a controlled feed rate of 0.5 ml per min with constant stirring until pH 2 was reached. The sol was stirred for 2 h and kept at room temperature for 24 h to complete the ageing process. The resultant gel was washed several times with ethanol and double distilled water and dried in an oven at 80°C for 24 h. After grinding, the synthesized powder was calcined at 400 and 600°C for 2 h [16]. For Nd^{3+}-doped samples calculated amount of $Nd(NO_3)_3 \cdot 6H_2O$ was added before the addition of ammonia solution. For a doped sample of 0.28%, the stannic chloride solution (5.8 g of $SnCl_4 \cdot 5H_2O$ in 50 ml) and neodymium nitrate solution (0.017 g of $Nd(NO_3)_3 \cdot 6H_2O$ in 20 ml) were prepared separately in ultrapure water. The neodymium nitrate solution was then quantitatively transferred into stannic chloride solution and made up to 100 ml using ultrapure water.

2.3 *Characterization*

The X-ray diffraction (XRD) patterns were recorded with Bruker Advance diffractometer using CuKα ($\lambda = 1.5406$ Å) radiation in 2θ ranging from 20° to 80° at a scanning rate of 0.02°/s. The morphology, particle size and structure of the synthesized samples were examined by transmission electron microscopy (TEM) and high-resolution TEM (HRTEM), using Philips-FEI Tecnai G2S-Twin. The specific surface area of pure and doped samples was determined from the adsorption isotherm of nitrogen at 77 K on the basis of the Brunauer–Emmett–Teller (BET) method using a micrometrics Gemini 2375, after degassing the samples at 200°C for 2 h. Diffuse reflectance spectra (DRS) of all the samples were recorded in the wavelength region of 200–800 nm

using Perkin Elmer Lambda 35 to study the optical absorption properties of photocatalysts. The chemical composition of the doped samples was determined from energy-dispersive spectrum (EDS) using Horiba EMAX operated at 137 eV.

2.4 *Photocatalytic measurements*

The photocatalytic efficiency of pure and doped samples was determined by the degradation of MB under sunlight. The whole experiments were carried out on a hot sunny day with a maximum temperature of 36°C. The intensity of solar radiation was in the range of 700–1010 W m^{-2}. The decolourization of MB was taken as a model reaction for evaluating the photocatalytic activity of all the samples. In a typical experiment, 50 mg of photocatalyst was added to 100 ml of 10 µmol MB solution and the solution was sonicated for 10 min by ultrasonic vibration. The suspension was kept in the dark for 30 min under continuous stirring to establish an adsorption/desorption equilibrium between the photocatalyst and the dye. The solution was then kept under sunlight with constant stirring and sampling was carried out at regular time intervals (1 h), centrifuged at 5000 r.p.m. to remove any sediment. The change in MB concentration with irradiation time was determined by measuring absorbance at 665 nm with a UV–visible spectrophotometer. The efficiency of the photocatalysts in the photodegradation of MB under sunlight exposure was calculated using the formula

$$\%D = \frac{(C_0 - C)}{C_0} \times 100,$$

where C_0 is the initial concentration of MB solution and C its concentration at different intervals of irradiation time.

3. Results and discussion

3.1 *Characterization of the photocatalysts*

Figure 1 shows the XRD patterns of pure and Nd^{3+}-doped tin oxide nanoparticles calcined at 400 and 600°C synthesized by the sol–gel method. All the samples are identified as tetragonal rutile-type SnO_2 phase with point group D_{4h}^{14} and space group $P4_2/mnm$ and the results are in good agreement with the standard JCPDS (Card no. 41-1445) data. Further, no characteristic peaks of impurities such as rare earth oxides or other tin oxides were observed in the XRD pattern showing the single-phase sample formation. The average crystallite size (d) of the sample was determined from the X-ray broadening line using Debye–Scherrer equation [21]:

$$d = 0.9\lambda/\beta \cos \theta,$$

where λ is the wavelength of the X-ray used and β the full-width at half-maximum (FWHM) of the peaks at the diffracting angle θ. The average crystallite size of the samples and the deviation, which is the standard deviation between the sizes estimated along the three different crystallographic

directions are given in table 1. As compared to pure SnO_2 calcined at 400°C, broadening of diffraction peaks and degradation of crystallinity can be observed with the increase in rare earth content, for the samples which were calcined at the same temperature [22]. This implies the reduction in crystallite size and can be attributed to the presence of Nd–O–Sn in the doped samples, which hinder the growth of SnO_2 particle to some degree. The lattice parameters of the samples are calculated by using the (110) and (101) peaks in the XRD pattern using the relations [23]

$$a = \sqrt{2}d_{110},$$

$$c = \frac{ad_{101}}{\sqrt{a^2 - d_{101}^2}},$$

where a and c are the lattice parameters and d the interplanar distance. The lattice parameters obtained are given in table 1. The increase in lattice parameters with the increase in Nd^{3+} ion shows that Nd^{3+} is successfully incorporated into the SnO_2 lattice [14]. Moreover, as ionic radius of Nd^{3+}

(0.108 nm) is larger than that of Sn^{4+} (0.069 nm), it is expected that Nd^{3+} interstitially substitutes the Sn^{4+} ion sites. Krishnakumar *et al* [24] prepared antimony-doped tin oxide nanostructures through the chemical precipitation technique and they found that the lattice parameters were increased when Sb^{3+} ions (ionic radius = 0.090 nm) substituted Sn^{4+} ions (ionic radius = 0.069 nm). Similar results were reported for rare earth-doped TiO_2 nanoparticles [25,26]. In the case of pure and 0.38% Nd^{3+}-doped SnO_2 samples calcined at 600°C, the crystallinity and crystallite size were increased as compared to the samples calcined at 400°C because calcination temperature plays a crucial role in improving the crystallinity of the samples [27].

The TEM image of 0.38% Nd^{3+}-doped SnO_2 nanoparticles is presented in figure 2a and the particle size distribution with lognormal profile and SAED patterns in its inset, and figure 2b shows the corresponding HRTEM image. Nearly spherical-shaped particles can be observed in TEM image and the SAED patterns exhibit the polycrystalline nature of the sample, which could be well-indexed to diffractions from the (110), (101) and (211) planes of the tetragonal rutile structure. From the TEM image the average particle size and the size distribution were estimated by lognormal curve fitting to the observed histograms. The crystallite size and average particle size obtained from XRD and TEM analyses for all the samples are depicted in table 1. It can be observed that the size of nanoparticles obtained from the TEM images is in close agreement with those obtained from XRD patterns. HRTEM image clearly reveal the lattice planes with a d-spacing of about 0.34 nm, which corresponds to the (110) planes of SnO_2. Hence the interplanar distances measured from HRTEM image agree well with the data obtained from XRD pattern.

EDS spectra of 0.38% Nd^{3+}-doped SnO_2 nanoparticles are shown in figure 3, which confirms the existence of Nd^{3+} ions in doped samples. Thus the successful doping of Nd^{3+} ions in SnO_2 is confirmed from EDS and XRD analysis.

Figure 4 shows the N_2 adsorption/desorption isotherms of pure and 0.38% Nd^{3+}-doped SnO_2 nanoparticles calcined at 600°C. They exhibit type IV isotherms with a H3-type hysteresis loop observed in the relative pressure (p/p_0) range of 0.6–0.95, revealing the characteristic of mesoporous materials. The specific surface area of pure and 0.38% Nd^{3+}-doped samples calcined at 600°C were determined to be 16 and 28 $m^2\ g^{-1}$.
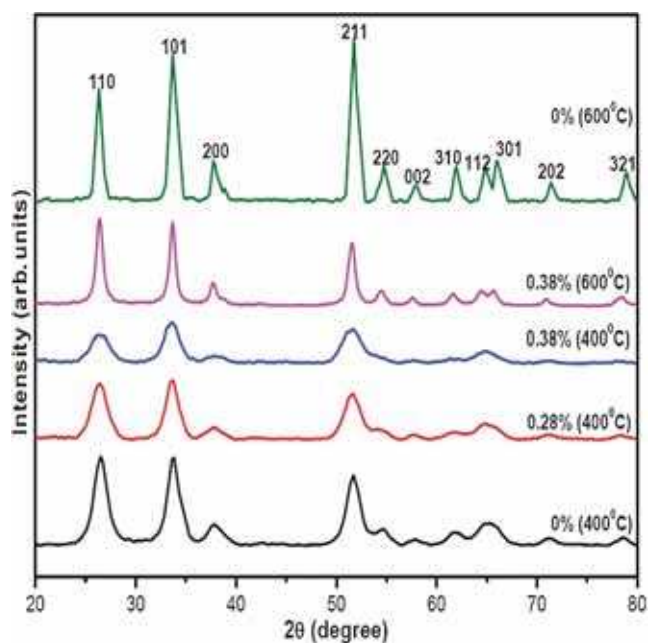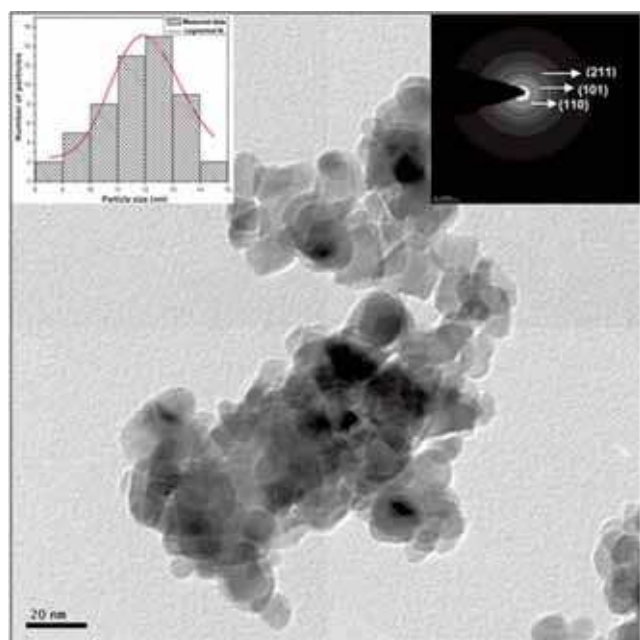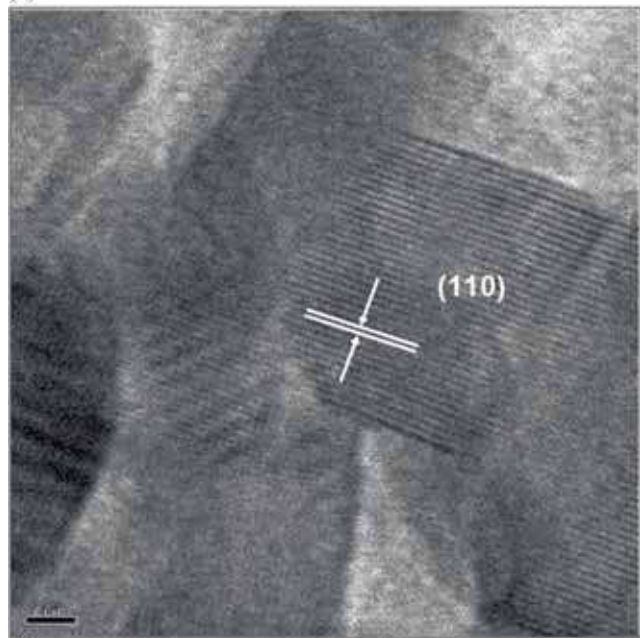

Figure 1. XRD patterns of pure and Nd^{3+}-doped SnO_2 calcined at 400 and 600°C.

Table 1. Comparison of particle size and lattice parameters of pure and doped SnO_2 nanoparticles.

Temperature (°C)	Concentration of Nd (%)	Size from Scherrer equation (nm)	Lattice parameter, a (nm)	Lattice parameter, c (nm)	Size from TEM analysis (nm)
400	0	6.97 ± 0.62	4.7403	3.1993	7.63 ± 0.70
400	0.28	5.36 ± 0.58	4.7800	3.1997	5.60 ± 0.58
400	0.38	4.32 ± 0.41	4.7869	3.2104	4.68 ± 0.56
600	0	14.98 ± 0.56	4.7852	3.2093	15.12 ± 0.43
600	0.38	11.74 ± 0.56	4.7842	3.2112	12.13 ± 0.96

Figure 2. (**a**) TEM image, inset showing the particle size distribution with lognormal profile and SAED patterns and (**b**) HRTEM image of 0.38% Nd^{3+}-doped SnO_2 nanoparticles calcined at 600°C.

Figure 3. EDS spectra of 0.38% Nd^{3+}-doped SnO_2 nanopowder.

Figure 4. N_2 adsorption/desorption isotherms of pure and 0.38% Nd^{3+}-doped SnO_2 nanoparticles calcined at 600°C.

Figure 5 shows the optical absorption spectra of pure and doped samples obtained by UV–visible diffuse reflectance in the range 200–800 nm, calcined at temperatures 400 and 600°C. As the doping percentage of neodymium and calcination temperature increases, the absorption edge shifts towards longer wavelength or lower energies. The red shift in the optical absorption edge of doped samples can be explained on the basis of charge transfer transition between f electrons of $N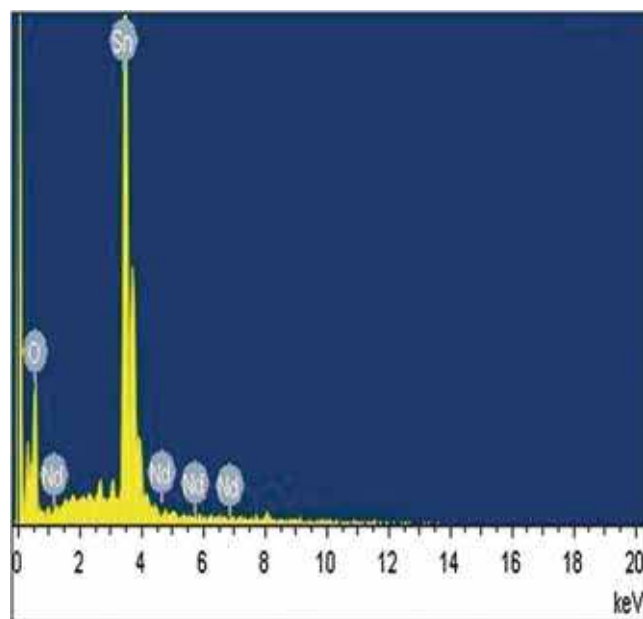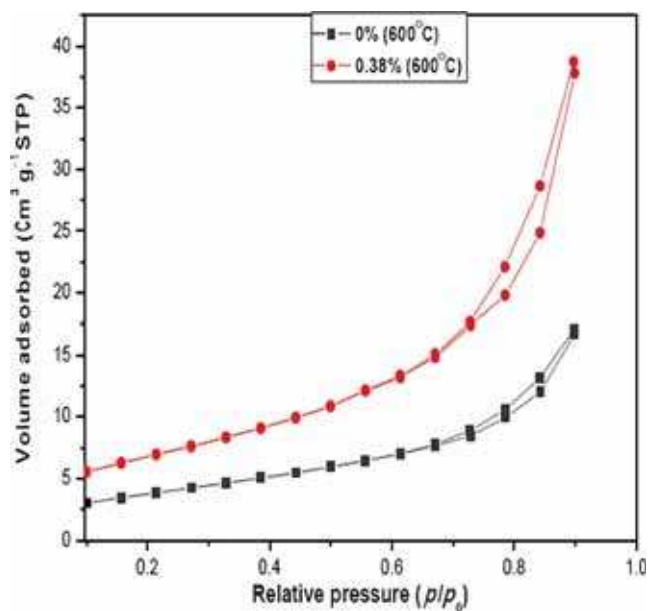d^{3+}$ ions and the SnO_2 conduction or valence band [25]. The absorption spectrum of 0.38% Nd^{3+}-doped SnO_2 calcined at 600°C have absorption bands at 583 and 746 nm which further confirms the visible-light absorbability of the photocatalyst and these peaks can be attributed to the 4f electron transitions of Nd^{3+} ions [25,28].

The variation of $(\alpha E_{bg})^2$ *vs.* E_{bg} for all the samples is shown in figure 6, where α is the absorption coefficient and E_{bg} is the photon energy. The optical band gap of the photocatalysts was obtained by extrapolating the linear portion of $(\alpha E_{bg})^2$ *vs.* E_{bg} plot to $\alpha = 0$. The decrease in band gap value
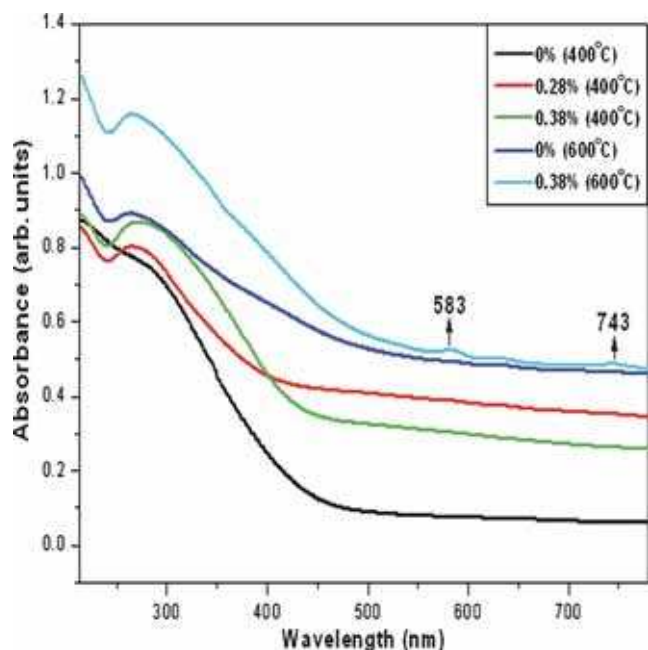
Figure 5. UV–visible spectra of pure and Nd^{3+}-doped SnO$_2$ calcined at 400 and 600°C.
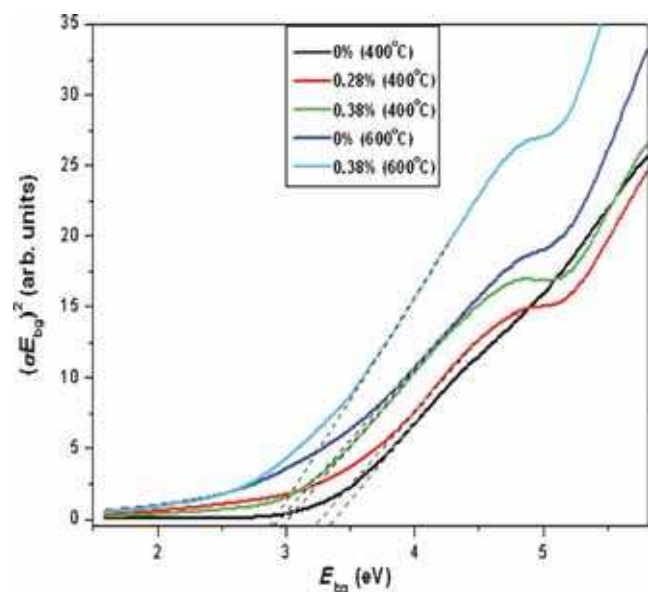

Figure 6. Band gap energy of pure and Nd^{3+}-doped SnO$_2$ calcined at 400 and 600°C.

with neodymium content and calcination temperature is summarized in table 2. In pure SnO$_2$, it was found that the band gap decreases with the increase in calcination temperature which is due to the increase in particle size [29]. Santara *et al* [30] studied the optical properties of undoped TiO$_2$ nanoribbons and found that samples grown at higher temperature followed by calcination at high temperature possess higher concentration of defects that is largely responsible for reduction in the bandgap. Ahmed *et al* [31] reported the band gap narrowing of nickel-doped SnO$_2$ nanoparticles prepared through the sol–gel method. They observed appreciable reduction in the band gap when the concentration of Ni was above 5% and attributed it as the formation of defect sub-bands below the conduction band. In our case, band gap narrowing can be attributed to the substitution of Nd^{3+} ions which introduced electron states into the band gap of SnO$_2$ to form the new lowest unoccupied molecular orbital [14]. Similar effect has been observed in rare earth-doped TiO$_2$ nanoparticles [32,33]. This would have played an important role for the enhancement of photocatalytic activity in Nd^{3+}-doped samples.

3.2 *Photocatalytic studies*

When a photocatalyst is irradiated with light having energy equal to or greater than its band gap energy ($h\nu \geq E_{gb}$), then electrons migrate from valence band (VB) to conduction band (CB) and holes are formed in VB. The photogenerated holes and electrons then undergo oxidation and reduction process with water and dissolved oxygen, results in the generation of hydroxyl radicals ($^{\bullet}$OH) and superoxide radical anions ($^{\bullet}$O$_2^-$), which are responsible for the degradation of organic dyes. Thus photogenerated electrons and holes play an important role in the degradation of organic dyes to nontoxic byproducts. However, the majority of photogenerated charge carriers have a chance for recombination, dissipating energy in the form of unproductive heat. The incorporation of rare earth ions into SnO$_2$ matrix introduces new energy levels which can either accept electrons from the VB or donate electrons to the CB, there by minimizes the recombination rate by the effective separation of electron–hole pairs [14]. Thus if charge separation is maintained then the charge carriers will reach the surface of the catalyst and degrade the dye.
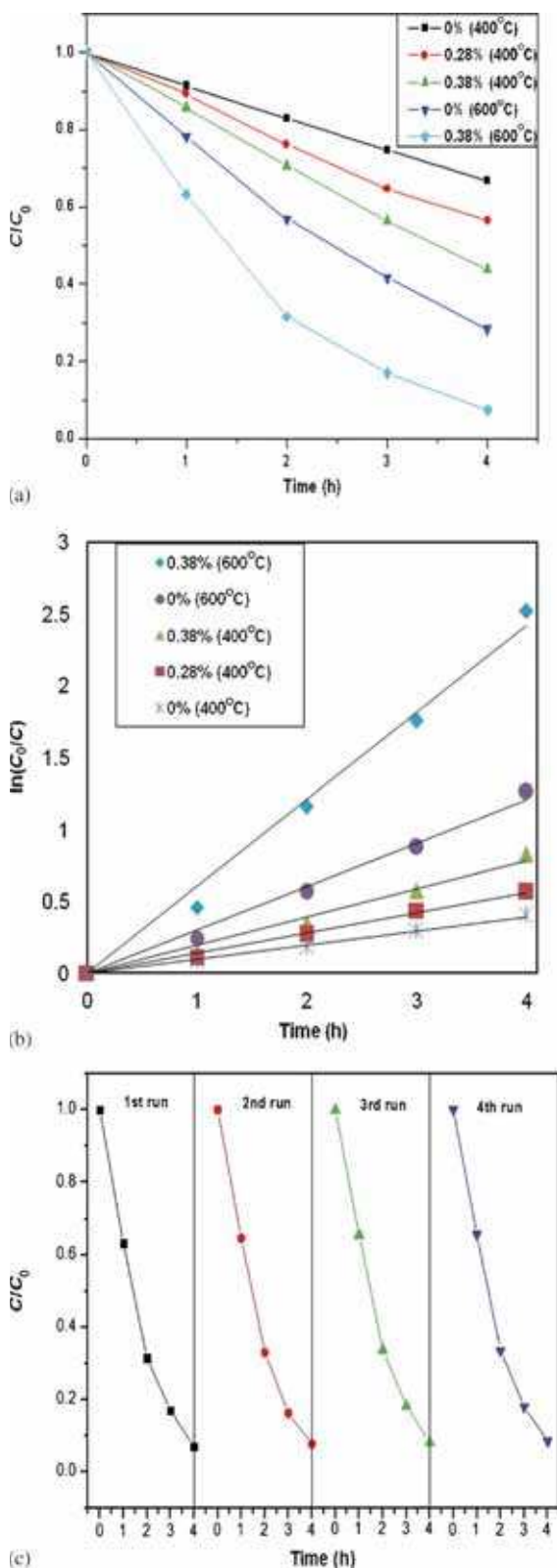
Table 2. Comparison of band gap energy, rate constant and photocatalytic degradation efficiency of pure and Nd^{3+}-doped SnO$_2$ calcined at 400 and 600°C.

Temperature (°C)	Concentration of Nd (%)	Band gap (eV)	Rate constant, k (h^{-1})	R^2	Photocatalytic degradation efficiency (%D) at $t = 4$ h
400	0	3.34	0.098	0.997	33.1
400	0.28	3.23	0.141	0.994	47.2
400	0.38	2.97	0.195	0.986	58.8
600	0	2.90	0.301	0.991	71.7
600	0.38	2.88	0.615	0.986	93.1

(a)

(b)

(c)

Figure 7. (**a**) Effect of Nd^{3+} doping concentration and calcination temperature on the degradation of MB solution in the presence of pure and Nd^{3+}-doped SnO_2 calcined at 400 and 600°C; (**b**) kinetic fit for the degradation of MB with pure and Nd^{3+}-doped SnO_2 calcined at 400 and 600°C; and (**c**) stability test for 0.38% Nd^{3+}-doped SnO_2 nanoparticles calcined at 600°C for four runs.

Figure 7a presents the effect of Nd^{3+} doping concentration and calcination temperature on the degradation of MB. The degradation of dye is drastically increased for the samples calcined at 600°C in comparison to 400°C. Many published reports [6,15,34,35] emphasize the importance of increased surface area in enhancing the photocatalytic activity. However, a catalyst with large surface area is sometimes associated with increased amount of crystalline defect which favour the recombination of electrons and holes and hence reduces the reaction rate [36,37]. Hence for effective charge separation not only the surface area, but also the crystallinity plays a very important role. With the increase in calcination temperature the crystallinity of the photocatalysts increases which result in the enhancement of the number of active sites for the degradation reactions, thereby increases the photocatalytic activity [38–41].

The plot of $\ln(C_0/C)$ *vs.* time is shown in figure 7b. The linear relationship of the plot of $\ln(C_0/C)$ *vs.* time indicates that the photodegradation of the dye obeys pseudo-first-order kinetics and the rate expression is given by the equation [34,42,43],

$$\ln\left(\frac{C_0}{C}\right) = kt,$$

where k is the pseudo-first-order rate constant, C_0 and C the concentration at time $t = 0$ and t, respectively. The pseudo-first-order rate constants (k) of all the photocatalysts obtained from the plot of $\ln(C_0/C)$ with time and linear regression coefficients (R^2) are given in table 2. The rate constants obtained clearly indicates that the photocatalytic activity of 0.38% Nd^{3+}-doped SnO_2 nanoparticles calcined at 600°C had faster dye degradation of 3.2 times than the same percentage calcined at 400°C and about 2 times that of the pure one calcined at 600°C. The stability tests of the photocatalytic activity of 0.38% Nd^{3+}-doped SnO_2 nanoparticles calcined at 600°C for four runs are shown in figure 7c. The results clearly indicated that the photocatalyst was stable even after four runs without any significant loss of photocatalytic activity, showing its efficiency for the degradation of organic pollutants. Hence in the present study we observed that reduction in electron–hole recombination as a result of charge separation maintained by doping SnO_2 with Nd^{3+} ions and band gap narrowing, can be attributed to the enhanced photocatalytic activity of Nd^{3+}-doped SnO_2 nanocatalysts.

4. Conclusions

Pure and Nd^{3+}-doped tin oxide nanoparticles were successfully synthesized by the sol–gel method. The XRD study reveals that the structure of the samples is tetragonal rutile-type SnO_2 phase and the sizes are found to decrease with the increase in doping percentage. Band gap narrowing was observed in Nd^{3+}-doped samples, which can be attributed to the substitution of Nd^{3+} ions which in effect introduced new electron states in the band gap of SnO_2 to form a new lowest

unoccupied molecular orbital. The photocatalytic efficiency of pure and doped samples was determined by the degradation of MB solution under day light illumination. It was found that the photocatalytic activity of SnO$_2$ is significantly enhanced by Nd^{3+} doping because the incorporation of Nd^{3+} into SnO$_2$ lattice reduces the band gap and inhibits electron–hole recombination so that visible light is sufficient to excite electrons from valence band to conduction band. The stability of the photocatalyst remains effective even after four runs, indicating its excellent photocatalytic activity for the treatment of industrial waste water containing dye effluents.

Acknowledgements

References

[1] Houas A, Lachheb H, Ksibi M, Elaloui E, Guillard C and Herrmann J M 2001 *Appl. Catal. B: Environ.* **31** 145

[2] Yu K S, Shi J Y, Zhang Z L, Liang Y M and Liu W 2013 *J. Nanomater.* **2013** 372951

[3] Ba-Abbad M M, Kadhum A A, Mohamad A B, Takriff M S and Sopian K 2013 *Chemosphere* **91** 1604

[4] Nair P B, Justinvictor V B, Daniel G P, Joy K, Ramakrishnan V, Kumar D D and Thomas P V 2014 *J. Thin Solid Films* **550** 121

[5] Narayana R L, Matheswaran M, Aziz A A and Saravanan P 2010 *Desalination* **269** 249

[6] Kuriakose S, Choudhary V, Satpati B and Mohapatra S 2014 *Beil. J. Nanotechnol.* **5** 639

[7] Begum N S, Ahmed H M F and Gunashekar K R 2008 *Bull. Mater. Sci.* **31** 747

[8] Vinodgopal K and Kamat P V 1995 *Environ. Sci. Technol.* **29** 841

[9] Bhosale R, Pujari S, Muley G, Pagare B and Gambhire A 2013 *J. Nanostruct. Chem.* **3** 1

[10] Vaezi M R and Sadrnezhaad K 2007 *Mater. Sci. Eng. B* **140** 73

[11] Luo L B, Liang F X and Jie J S 2011 *Nanotechnology* **22** 485701

[12] Birkel A, Lee Y G, Koll D, Meerbeek X V, Frank S, Choi M J, Kang Y S, Char K and Tremel W 2012 *Energy Environ. Sci.* **5** 5392

[13] Jiang L Y, Wu X L, Guo Y G and Wan L J 2009 *J. Phys. Chem. C* **113** 14213

[14] Singh L P, Luwang M N and Srivastava S K 2014 *New J. Chem.* **38** 115

[15] Foletto E L, Battiston S, Collazzo G C, Bassaco M M and Mazutti M A 2012 *Water Air Soil Pollut.* **223** 5773

[16] Adnan R, Razana N A, Rahman I A and Farrukh M A 2010 *J. Chin. Chem. Soc.* **57** 222

[17] Niasari M S, Mir N and Davar F 2010 *Inorg. Chim. Acta* **363** 1719

[18] Saravanakumar M, Agilan S, Muthukumarasamy N, Marusamy A, Prabaharan K, Ranjitha A and Uma Maheshwari P 2014 *Indian J. Phys.* **88** 831

[19] Das S, Kar S and Chaudhuri S 2006 *J. Appl. Phys.* **99** 114303

[20] Yu F, Tang D, Hai K, Luo Z, Chen Y, He X, Peng Y, Yuan H, Zhao D and Yang Y 2010 *J. Cryst. Growth* **312** 220

[21] Cullity B D 1978 *Elements of X-ray diffraction* (Massachusetts: Addison-Wesley) 2nd ed

[22] Pillai S K, Sikhwivhilu L M and Hillie T K 2009 *Mater. Chem. Phys.* **120** 619

[23] Entradas T, Cabrita J F, Dalui S, Nunes M R, Monteiro O C and Silvestre A J 2014 *Mater. Chem. Phys.* **147** 563

[24] Krishnakumar T, Jayaprakash R, Pinna N, Phani A R, Passacantando M and Santucci S 2009 *J. Phys. Chem. Solids* **70** 993

[25] Stengl V, Bakardjieva S and Murafa N 2009 *Mater. Chem. Phys.* **114** 217

[26] Anandan S, Ikuma Y and Murugesan V 2012 *J. Photoenergy* **2012** 921412

[27] Bagheri-Mohagheghi M M, Shahtahmasebia N, Alinejada M R, Youssefic A and Shokooh-Saremid M 2008 *Physica B* **403** 2431

[28] Bokare A, Sanap A, Pai M, Sabharwal S and Athawale A A 2013 *Colloids Surf. B: Biointerface* **102** 273

[29] Bhagwat M, Shah P and Ramaswamy V 2003 *Mater. Lett.* **57** 1604

[30] Santara B, Giri P K, Imakita K and Fujii M 2013 *J. Phys. Chem. C* **117** 23402

[31] Ahmed A S, Muhamed S M, Singla M L, Tabassum S, Naqvi A H and Azam A 2011 *J. Lumin.* **131** 1

[32] Xiao Q, Si Z, Yu Z and Qiu G 2008 *J. Alloys Compd.* **450** 426

[33] Li W, Wang Y, Lin H, Shah S I, Huang C P, Doren D J, Rykov S A, Chen J G and Barteau M A 2003 *Appl. Phys. Lett.* **83** 4143

[34] Kuzhalosai V, Subash B, Senthilraja A, Dhatshanamurthi P and Shanthi M 2013 *Spectrosc. Acta A: Mol. Biomol. Spec.* **115** 876

[35] Behnajady M A and Tohidi Y 2014 *Photochem. Photobiol.* **90** 51

[36] Wang Q Q, Lin B, Xu B, Li X, Chen Z and Pian X 2010 *Microporous Mesoporous Mater.* **130** 344

[37] Hao H and Zhang J 2009 *Microporous Mesoporous Mater.* **121** 52

[38] Pouretedal H R, Shafeie A and Keshavarz M H 2012 *J. Korean Chem. Soc.* **56** 484

[39] Hamrouni A, Lachheb H and Houas A 2013 *Mater. Sci. Eng. B* **178** 1371

[40] Sifontes A B, Rosales M, Méndez F J, Oviedo O and Zoltan T 2013 *J. Nanomater.* **2013** 265797

[41] Ambreen S, Pandey N D, Mayer P and Pandey A 2014 *Beil. J. Nanotechnol.* **5** 1082

[42] Bandekar G, Rajurkar N S, Mulla I S, Mulik U P, Amalnerkar D P and Adhyapak P V 2014 *Appl. Nanosci.* **4** 199

[43] Haldorai Y and Shim J J 2014 *Polym. Compos.* **35** 327